A 30 nm-resolution hard X-ray microscope with X-ray fluorescence mapping capability at BSRF

Qingxi Yuan,[a] Kai Zhang,[a] Youli Hong,[a] Wanxia Huang,[a] Kun Gao,[b] Zhili Wang,[a] Peiping Zhu,[a] Jeff Gelb,[c] Andrei Tkachuk,[c] Benjamin Hornberger,[c] Michael Feser,[c] Wenbing Yun[c] and Ziyu Wu[a,b]*

[a]Beijing Synchrotron Radiation Facility, Institute of High Energy Physics, Chinese Academy of Sciences, Beijing 100049, People's Republic of China, [b]National Synchrotron Radiation Laboratory, University of Science and Technology of China, Hefei, Anhui 230026, People's Republic of China, and [c]Xradia Inc., 4385 Hopyard Road, Suite 100, Pleasanton, CA 94588, USA. E-mail: wuzy@ihep.ac.cn

A full-field transmission X-ray microscope (TXM) operating continuously from 5 keV to 12 keV with fluorescence mapping capability has been designed and constructed at the Beijing Synchrotron Radiation Facility, a first-generation synchrotron radiation facility operating at 2.5 GeV. Spatial resolution better than 30 nm has been demonstrated using a Siemens star pattern in both absorption mode and Zernike phase-contrast mode. A scanning-probe mode fluorescence mapping capability integrated with the TXM has been shown to provide 50 p.p.m. sensitivity for trace elements with a spatial resolution (limited by probing beam spot size) of 20 µm. The optics design, testing of spatial resolution and fluorescence sensitivity are presented here, including performance measurement results.

1. Introduction

In the recent past, full-field transmission X-ray microscopy (TXM) operating in the hard X-ray regime has undergone rapid improvements based on the development of highly efficient X-ray optics for that regime (Zeng *et al.*, 2008; Feng *et al.*, 2007; Tkachuk *et al.*, 2007). With outstanding high-throughput non-destructive three-dimensional imaging capabilities, TXM has attracted significant interest across many different disciplines. Many synchrotron radiation facilities have built this kind of hard X-ray microscope (Yin *et al.*, 2006; Andrews *et al.*, 2008; Chu *et al.*, 2008; Tian *et al.*, 2008) and made significant progress in this field (Chen *et al.*, 2011*a,b*; Yi *et al.*, 2011), along with a wide range of research work in biological (Andrews *et al.*, 2010*a,b*, 2011; Liu *et al.*, 2011*a*; Chen *et al.*, 2011*c*) and materials science fields (Chen *et al.*, 2008; Hsu *et al.*, 2010; Meirer *et al.*, 2011; Nelson *et al.*, 2011; Sun & Wang, 2011).

The TXM program at the Beijing Synchrotron Radiation Facility (BSRF) is driven by the needs of a diverse science community preferring a non-destructive high-resolution probe. Examples are the analysis of failure mechanisms in microelectronic devices due to electro-migration, thermal breakdown or inhomogeneity in the industry field, and the characterization of porous materials such as soils and rock as well as the investigation of the transportation behavior in these porous structures. In the field of biological applications, TXMs working in the soft X-ray region around 500 eV ('water window' region) provide strong contrast between organic matter and water and have shown outstanding results recently (Hertz *et al.*, 2012; Chichon *et al.*, 2012). However, water-window TXM is limited to small micrometre-size cells because of the limited penetration and depth of focus at these photon energies. Hard X-ray TXM provides more flexibility to image larger cells, tissue sections and bone, as well as non-biological materials as mentioned above. However, for soft materials, the use of phase contrast is required. All these potential applications of TXM promoted the design and construction process in 2007. In October 2010, the BSRF TXM was commissioned in the 5–12 keV X-ray energy range, demonstrating spatial resolution better than 30 nm. In addition to high-resolution two-dimensional and three-dimensional full-field imaging, a fluorescence mapping mode is implemented in this instrument. BSRF is the only first-generation parasitical synchrotron radiation facility known to the authors at the time of writing where correlative 30 nm spatial resolution and fluorescence mapping have been achieved with TXM. The solution has been developed in the context of the BSRF instrumentation development program for a wide range of applications in materials science and biological research.

research papers

2. Instrument design

2.1. General description of the instrument

The TXM instrument, shown in Fig. 1, has an optical layout similar to a visible-light microscope. The X-ray beam is focused onto the sample by a condenser consisting of an elliptically shaped capillary (Zeng *et al.*, 2008). Hereafter, the objective zone plate (Feng *et al.*, 2007) produces a magnified image of the sample on a scintillator crystal. The resulting visual image is then further enlarged with a microscope objective lens and captured by a 16-bit 1024×1024 CCD camera for imaging with resolution down to 30 nm. In addition, the TXM is equipped with a set of phase rings to enable Zernike phase-contrast imaging at the same resolution level at fixed X-ray energies of 5 keV, 8 keV and 11 keV. The choice of discrete energies for Zernike phase contrast is due to the required matching of ring illumination from the (achromatic) condenser and the phase ring in the back focal plane of the (chromatic) objective lens. Since phase contrast is typically not used for spectroscopic studies, a set of discrete energies is adequate for most experiments of interest. Note that Zernike phase contrast is not a quantitative phase-contrast imaging method, and a few methods have been presented to achieve quantitative phase recovery (Yin *et al.*, 2007; Liu *et al.*, 2011b).

The TXM is also designed with a mechanism that enables switching from the synchrotron X-ray source to a rotating-anode laboratory source. This developed dual-source concept extends the usable operating time of the microscope since BSRF operates in a parasitic mode and only provides synchrotron radiation for a short part of the year. The rotating-anode X-ray generator has switchable copper and chromium targets with operating energies of 8.0 keV (Cu K_α) and 5.4 keV (Cr K_α), respectively. The sample and most optical components (except for the scintillator, visual magnification system and camera) are located in a vacuum chamber to reduce air absorption at the lower end of the energy range and to allow for experiments requiring specific atmospheric conditions. A total of five separate capillary condenser optics with optimized parameters are available in the instrument to cover all imaging modes available with the rotating-anode laboratory source and synchrotron source. Three imaging zone plates are installed to cover the energy range 5–12 keV and different imaging modes of the TXM. All optics are motorized and configuration changes between imaging modes are executed automatically.

An ion chamber is installed before the condenser to normalize exposure time to beam intensity, which has been measured to decay over the time scale of a few hours. To minimize exposure of the sample to radiation when not imaging, a shutter is installed just after the ion chamber. The shutter can be automatically controlled by the software.

The support table is equipped with passive dampening to isolate floor vibrations. According to the survey, vibrations are not a concern as proven by the resolution achieved (<30 nm).

2.2. Choice of beamline parameters

At the BSRF TXM beamline, polychromatic radiation is delivered by the single-period wiggler (Jiang *et al.*, 1993) (wavelength shifter) 4W1 with a magnetic field strength of 1.8 T and critical energy of 7.5 keV. A focusing beamline scheme is chosen to maximize the efficiency of the coupling to the TXM capillary condenser.

A general requirement for a TXM beamline and condenser system is that the illumination fills the beam acceptance of the microscope, defined as the product of the field of view and the acceptance angle of the objective lens (equal to two times the numerical aperture). For beamlines at third-generation synchrotron sources, the beam emittance, defined as the product of beam size and beam divergence, is typically smaller than the TXM phase-space acceptance at least in the vertical plane and sometimes also in the horizontal plane. The common practice is to choose the parameters of the beamline and TXM condenser optics to match the illumination angle of the sample to the numerical aperture (NA) of the objective zone plate (critical illumination) and to homogeneously distribute the focused beam by raster-scanning the condenser optic, with a corresponding loss in average flux. As shown below, the provided phase space of the BSRF source overfills
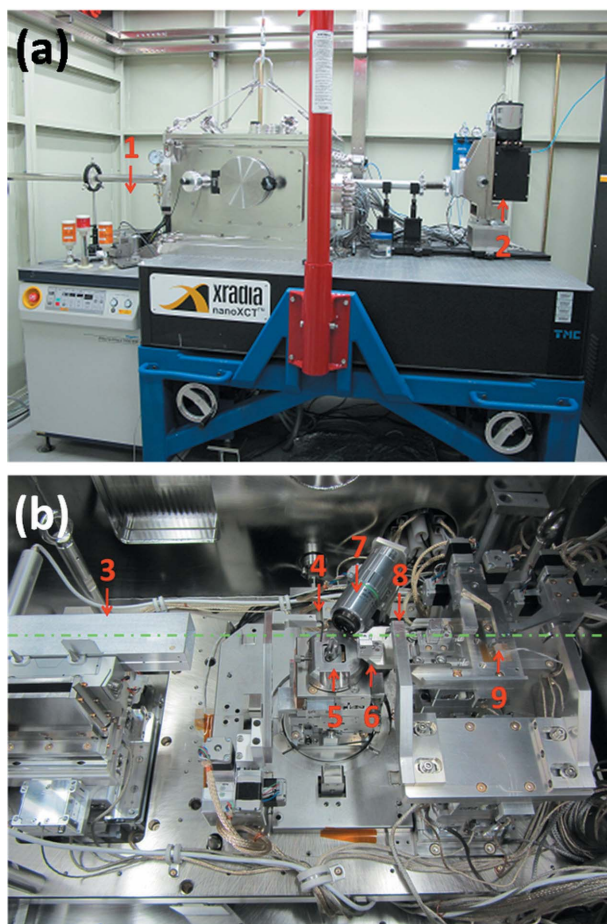
Figure 1
Photograph of (*a*) the BSRF TXM inside the hutch and (*b*) the TXM inside the vacuum chamber. 1, Laboratory X-ray source; 2, detector; 3, condenser; 4, pinhole; 5, sample stage; 6, zone plate; 7, visible-light microscope; 8, phase ring; 9, Bertrand lens.
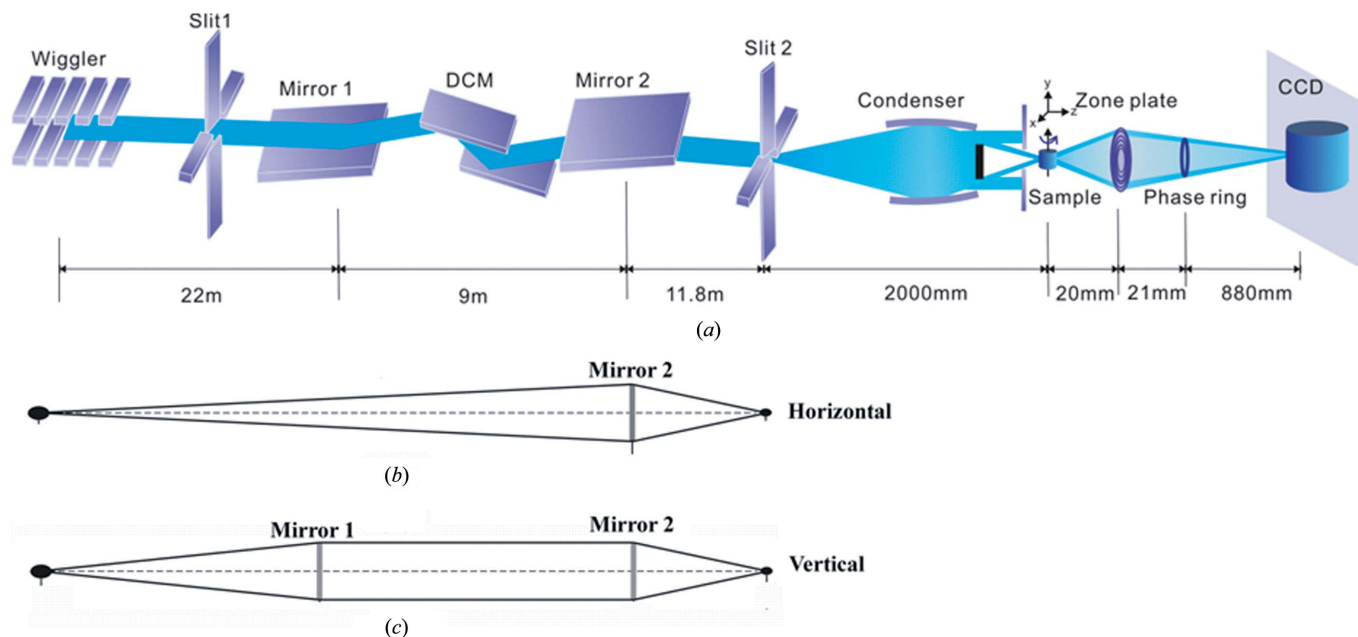
Figure 2
(*a*) Optical layout of the beamline and TXM at BSRF. (*b*) Horizontal focusing scheme. (*c*) Vertical focusing scheme.

the phase-space requirement of the microscope, avoiding the need for raster-scanning of the illumination. Note, however, that the total flux delivered into the microscope field of view is still significantly lower at a first-generation synchrotron than a similarly designed third-generation synchrotron beamline, emphasizing the need for a thorough design process for all optics.

In the case of the BSRF TXM, the beamline source size is 2.46 mm horizontally (H) × 0.84 mm vertically (V) (FWHM), and the beam divergence is 0.38 mrad (H) and 0.26 mrad (V) FWHM. To illustrate the design considerations, we first calculate the matching of the available beamline phase space to the required phase space of the microscope for the case of 8 keV X-rays. The optical layout of beamline and TXM is shown in Fig. 2.

As shown in Fig. 2(*a*), the synchrotron X-ray beam passing through slit 1 is collimated vertically by mirror 1 and then focused by the cylindrical bending mirror 2. A double-crystal monochromator with a pair of Si(111) crystals is set between the two mirrors and tunes the X-ray energy in the range 5–12 keV. As the secondary source, slit 2 is set at the focus point

of mirror 2. The Fresnel zone plate, installed after the sample position, serves as the objective imaging lens to produce a magnified image of the sample on the detector. When using the laboratory source, the laboratory source condenser illuminates the sample with a magnification factor of ∼1.

For zone-plate imaging, when illuminated by a parallel beam, the Rayleigh resolution is

$$\delta = 0.61\lambda/\mathrm{NA} = 1.22\Delta R_n. \tag{1}$$

According to Fig. 3, if the illumination is an inclined beam or hollow cone beam, the resolution δ on the sample obeys the Rayleigh criterion according to the following equation,

$$\delta = 0.61\lambda/2\theta = 0.61 f\lambda/D, \tag{2}$$

where f is the zone-plate focal length, D is the zone-plate diameter, λ is the X-ray wavelength, and 2θ is the angle deflected from the incident direction to the far side of the objective zone plate (two times the zone-plate numerical aperture, $\theta = \lambda/\Delta 2R_n$). Then we have

$$\delta = 0.61\Delta R_n. \tag{3}$$
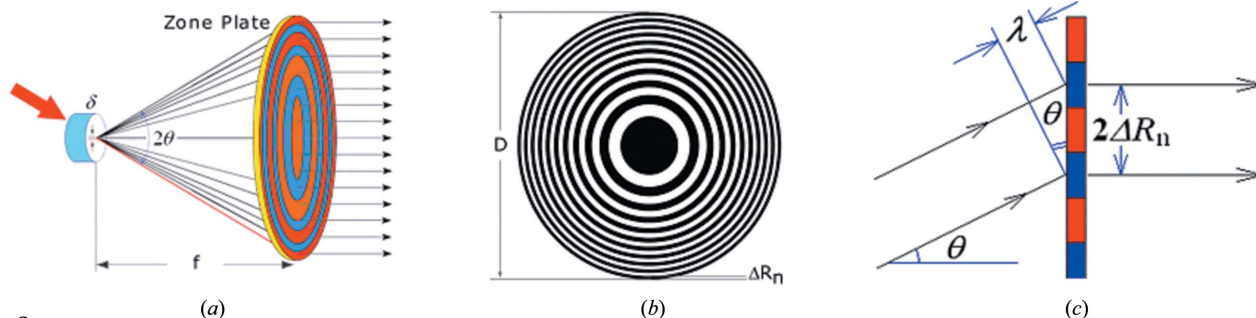
Figure 3
Illustration of (*a*) zone-plate imaging, (*b*) zone plate, (*c*) schematic for correlation about the zone-plate numerical aperture θ, X-ray wavelength λ and the outermost zone width ΔR_n.
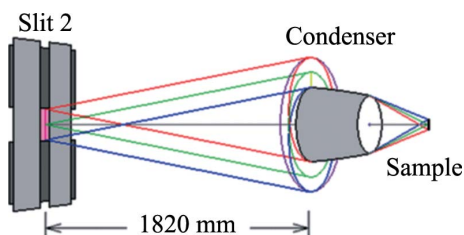
Figure 4
Schematic illustration of X-rays emerging from slit 2 to illuminate the condenser. X-rays from each point through the slit need to illuminate the whole input area of the condenser to provide a uniform illumination.

According to (3), for an objective zone plate with 40 nm outermost zone width, a spatial resolution of 24–25 nm can be expected.

Based on (2), if we want a spatial resolution of 30 nm we have to have $2\theta = 3.05$ mrad with 8 keV X-rays ($\lambda = 0.15$ nm). Therefore, for a 20 µm field of view the required phase space provided by the condenser at the sample position should be equivalent to 20 µm × 3 mrad or 60 µm mrad.

The demagnification factor of the condenser optics has been chosen to be 10 for the 8 keV condenser in synchrotron operation, which translates into a required phase space of 200 µm × 0.3 mrad for the secondary source (point of the optical axis at the position of slit 2). According to Fig. 4, it is necessary for the condenser to obtain the same phase-space illumination from every point of the secondary source away from the central optical axis. Therefore, the divergence requirement should be enlarged by 200 µm/1820 mm = 0.11 mrad (200 µm is the size of slit 2). This results in the total phase space needed at the secondary source of 200 µm × 0.41 mrad, which will be shown below to be satisfied by the synchrotron source properties and the choice of beamline optics. The slope errors of the reflective monocapillary condensers are typically below 100 µrad FWHM, which for a working distance around 200 mm translates to a blur in the imaging plane below 40 µm.

From Figs. 2(*b*) and 2(*c*) the demagnification factor of the beamline can be seen to be 31/11.8 horizontally and 22/11.8 vertically. Thus, we calculate the necessary phase space at the source to be 525 µm × 0.156 mrad (H) and 373 µm × 0.22 mrad (V). The phase space provided by the BSRF-4W1 source is 2460 µm × 0.38 mrad horizontally and 840 µm × 0.26 mrad vertically, which easily overfills the phase-space requirement of the TXM provided the mirrors do not clip the beam divergence.

The incidence angle of the X-ray beam on both mirrors has been chosen to be 5 mrad to cover the planned operating energy range of 5–12 keV. Both mirrors are Rh-coated to push the critical angle to 5.6 mrad at 12 keV. The length of both mirrors has been chosen to be 1000 mm with a usable length of 900 mm, which limits the vertical angular acceptance of the first mirror to 0.20 mrad, just meeting the requirement of the phase space intercepted from the source. Since the beam is parallel between mirrors 1 and 2, the second mirror intercepts the whole vertical beam as well. In the horizontal plane the mirror width of 40 mm exceeds the necessary calculated width of 4.84 mm on the second mirror by a wide margin.

According to the above calculations, slit 1 should be set to restrict the angular divergence of the beam to 0.2 mrad vertically and 0.156 mrad horizontally to eliminate unnecessary beam on the optical elements.

The above design is based on ideal conditions of each optical element. The imperfections of optical elements (slope errors) will increase the phase space of the X-ray beam during its propagating process through beamline and TXM, which increases the uniformity of the illumination in the sample plane at the expense of flux density.

2.3. Design for using both synchrotron and laboratory source

As a parasitic facility, the beam time for BSRF for user operation is limited currently to three to four months per year. In order to fully utilize the instrument, a laboratory rotating-anode X-ray source with swappable copper and chromium target (Tkachuk *et al.*, 2007) with 70 µm spot size was implemented in the BSRF-TXM. This source is on a manually operated stage and can be inserted into the beam path when the synchrotron does not supply X-ray beam (Wu *et al.*, 2010).

In order to properly focus the beam at the same sample position, two different types of condensers were designed, one set for the synchrotron beam and the other set for the laboratory source, as shown in Fig. 5. The focusing conjugates of these condensers are significantly different. In the case of the synchrotron beam, the distance between the secondary source (slit 2) and the capillary condenser is 2 m and the condenser demagnifies the source by ten times. In the case of the laboratory source, the condenser is a 1:1 focusing lens with a conjugate distance between source and sample of 0.5 m only. This is chosen to most effectively utilize each X-ray source, appropriately filling a large field of view on the sample plane while simultaneously providing high spatial resolution.

2.4. Design for fluorescence capability

The ability to collect an X-ray fluorescence signal from the sample has been integrated into the design of the instrument.
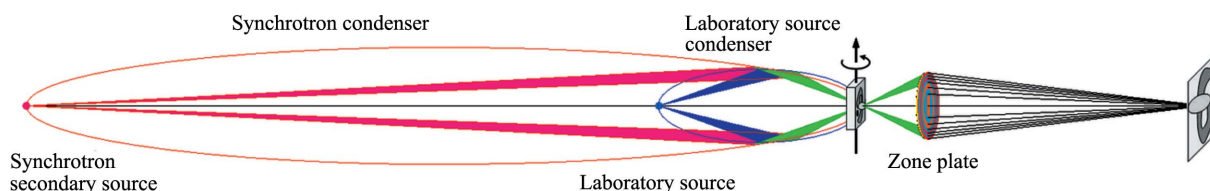
Figure 5
Design of the laboratory source condenser and synchrotron source condenser.

Based on the described design, the TXM condenser illuminates a field of view of approximately 20 µm × 20 µm at the sample position. Although this size is not comparable with micrometre or even submicrometre spots achieved by dedicated state-of-the-art fluorescence instruments existing in many synchrotron facilities, it is still very useful for users to measure the elemental composition within the field of view in addition to taking high-resolution images. Additionally, a raster scan of the sample can provide a coarse-resolution X-ray fluorescence map of an extended sample area. For fluorescence operation, a Si(Li) detector (model XR-100CR, Amptek) is placed perpendicular to the TXM optical axis as EDS detector to minimize the contribution to the signal by elastic scattering. The software allows data acquisition for X-ray fluorescence to be run concurrently with the TXM control software.

3. Instrument performance

3.1. Photon flux

The photon flux of the beamline just before slit 2 has been measured using an ion chamber to be about 3×10^{10} photons s^{-1} at 8 keV. A measurement after the slit with the slit setting typically used for imaging is not available at the time of writing.

For a typical flat-field image (no sample) with 15 nm pixel size, we measure about 200 camera counts per second per pixel without pixel binning. Using a calibration of 16 camera counts per 8 keV X-ray photon (as measured previously for an equivalent scintillator/optics/camera set-up using a large-area photon-counting detector) and 12% measured efficiency for the first diffraction order of the 1400 nm-thick double-stacked zone plate (Feng *et al.*, 2007; Chen *et al.*, 2008), this results in a total photon flux of about 100 photons s^{-1} pixel^{-1} in the sample plane. Comparing this with the flux of 3×10^{10} photons s^{-1} before slit 2 and considering the image size of 1024 × 1024 pixels, the effective transmission of the slit/condenser system to the image plane is about 3.5×10^{-3}. Part of this loss of flux is due to intentional blockage by the slits and central stop on the condenser (which is needed to provide hollow cone illumination, see Fig. 2, and for the condenser used covers about 80% of the condenser area), as well as the known condenser reflectivity of about 80%. The remaining losses are possibly due to illumination spread outside the condenser aperture or outside the imaged area in the sample plane.

Typical exposure times without pixel binning are about 90–120 s per two-dimensional radiograph using 8 keV synchrotron radiation X-rays. Using 181 radiographs at 90 s per view will result in a total exposure time of about 5.5 h in synchrotron operation mode (scaling exposure time to match ion chamber current) for a full tomogram. Depending on the experimental requirements, the exposure time can be reduced by using pixel binning, with a corresponding loss of pixel resolution.

Comparing the camera counts in flat-field images, the laboratory source with its dedicated condenser provides about 10% of the flux of the synchrotron in the sample plane.
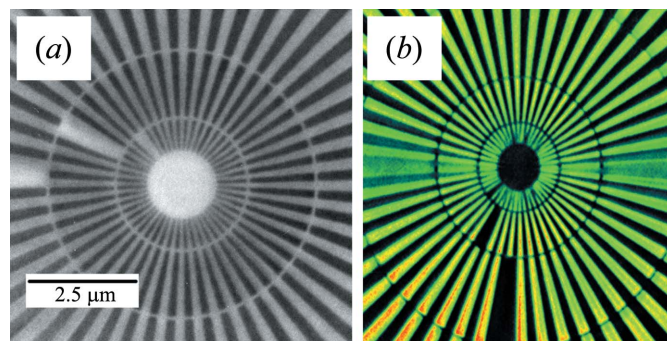
Figure 6
(*a*) Two-dimensional image and (*b*) rendering of a three-dimensional tomographic volume of a Siemens star resolution test target with 50 nm finest features imaged using the laboratory source operating at 8 keV.

3.2. TXM spatial resolution

The spatial resolution was tested by imaging an electroplated gold star pattern with the laboratory X-ray source and with the synchrotron beam.

With the laboratory source using the copper target (8.0 keV), a Siemens star with 50 nm finest features was imaged in two-dimensions as well as three-dimensions using a zone plate with 40 nm outermost zone width. A total of 121 sequential radiographs were acquired over an angular rotation range of 120° with an exposure time of 900 s for each radiograph and a pixel size of 15 nm. Tomographic reconstruction was performed using a filtered backprojection algorithm. The results shown in Fig. 6 indicate that both two-dimensional and three-dimensional spatial resolution of 50 nm have been achieved for the laboratory X-ray source, limited by the large spectral bandwidth of the Cu $K\alpha$ emission, which introduces chromatic aberration.

For the synchrotron beam, TXM spatial resolution was tested both in absorption and Zernike phase-contrast mode. Fig. 7(*a*) shows an absorption image taken at 8 keV of a star pattern with features tapering to a 30 nm minimum feature size at the centre of the pattern. Fig. 7(*b*) is a Zernike phase-contrast image taken at 8 keV of the same star pattern. Fig. 7(*c*) shows an absorption image taken at 8 keV of another star pattern with 24 nm minimum feature size at the centre. A more accurate analysis of the whole area of Fig. 7(*c*) using the accepted technique (Wang *et al.*, 2012; Yi *et al.*, 2011; Chen *et al.*, 2011*a*,*b*) of radial power spectrum density (RPSD) is shown in Fig. 7(*d*). It can be seen that the power spectrum of the sample cuts off at a spatial frequency of 19 µm^{-1}, corresponding to a period of about 52 nm. Thus, the TXM spatial resolution, which is usually represented by half the spatial period (line width), can be concluded to be 26 nm.
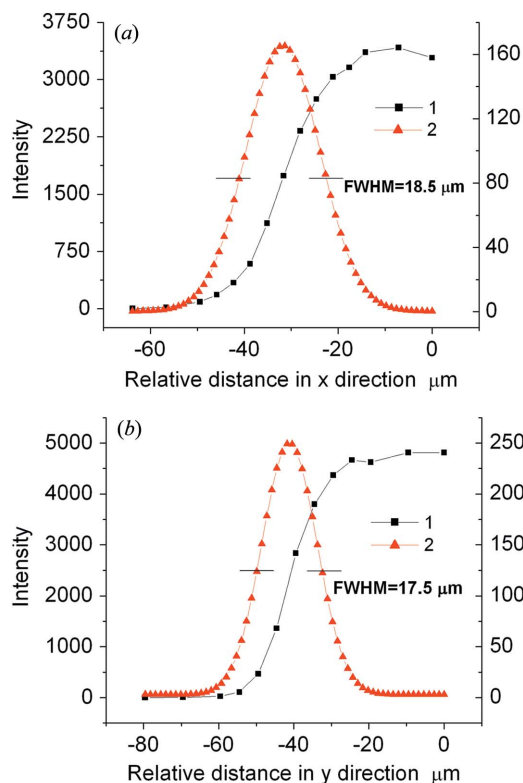
3.3. Fluorescence capability

X-ray fluorescence analysis offers elemental analysis with high sensitivity (Gordon, 1982), which allows the role of trace elements to be investigated in the function of biological systems. According to the blade scan results shown in Fig. 8, with slit 2 set at 200 µm × 200 µm, the condenser focal spot
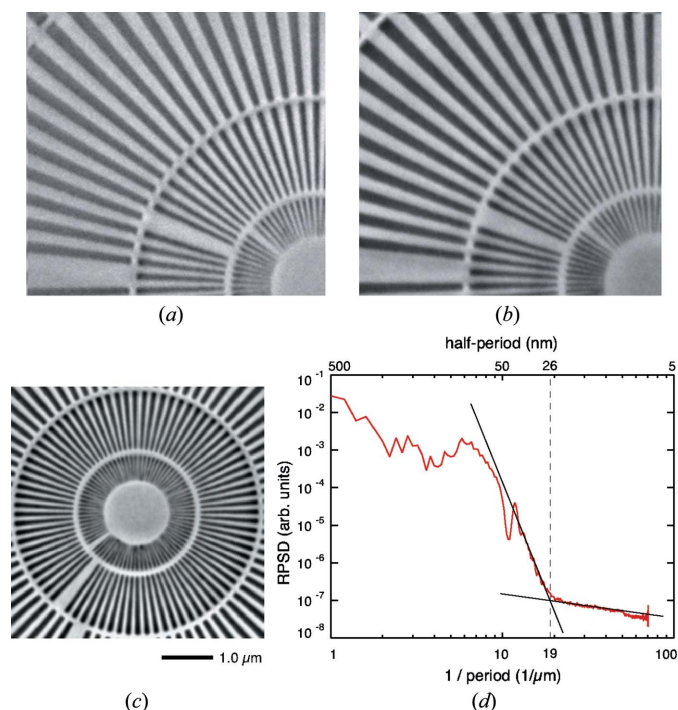
Figure 7
Image taken at 8 keV with star pattern features tapering to 30 nm in (*a*) absorption mode and (*b*) Zernike phase-contrast mode. (*c*) Image of a star pattern with features tapering to 24 nm taken at 8 keV in absorption mode. (*d*) RPSD analysis of (*c*). RPSD was created by rolling-off the image edges across a width of 40 pixels to avoid discontinuities for the Fourier transform.

Figure 8
Blade-scanning results of the condenser focal spot in (*a*) the *x* direction and (*b*) the *y* direction with slit 2 set at 200 µm × 200 µm. Line 1 is the original data and line 2 is the Gaussian fitting result of the derivative of the original data.

size at the sample plane is about 18.5 µm × 17.5 µm (FWHM), which can be used to carry out fluorescent mapping experiments while acquiring images.

To assess the sensitivity and detection limit of the X-ray fluorescence mode, a trace-element analysis experiment was performed using the number 612 standard sample from US National Institute of Standards and Technology (NIST), whose nominal trace-element concentration is 50 p.p.m. The 'fluorescence spectra with elements' emission line series, including the *K* or *L* series, as shown in Fig. 9, were fitted with *PyMCA* (Solé *et al.*, 2007) freely provided by the software group of ESRF for interactive data processing. Excitation lines with energies lower than 1 keV cannot be detected with good signal-to-noise ratio owing to absorption of the air path of about 5 cm. Note that a 5 cm air path before the fluorescence detector only existed at the time of commissioning when the fluorescence sensitivity was tested. Right now, the fluorescence detector can be put in the whole vacuum system. The fitting results match with elements given by NIST (including the Ar *K* peak 2.9 keV, which exists in the air). Thus, we conclude that the fluorescence sensitivity of the BSRF TXM is substantially better than 50 p.p.m, since

the peaks are very nicely resolved indicating that lower concentrations of the elements of interest would still be readily detectable.

4. Initial applications examples

The first sample imaged with BSRF-TXM is shale as shown in Fig. 10. Shale is typically composed of variable amounts of clay minerals and quartz grains. The oil and gas industry is now looking toward shale as a source of stored hydrocarbons,
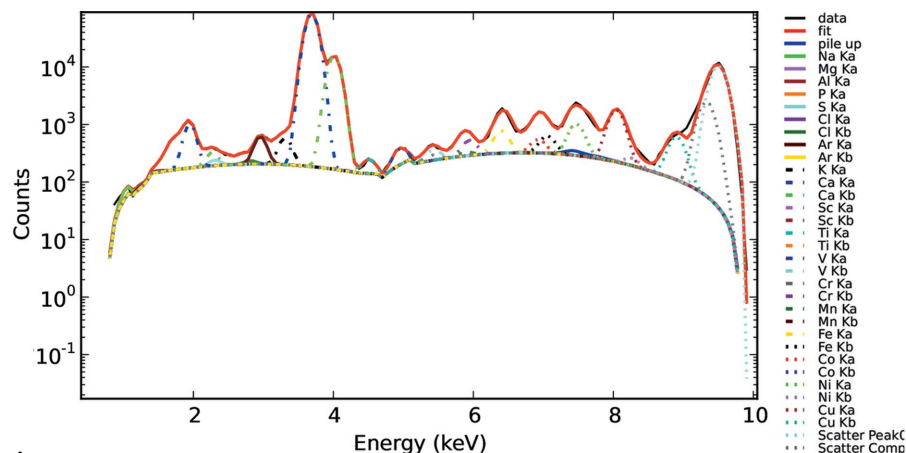
Figure 9
Fluorescence spectrum of standard sample 612 from NIST acquired with the BSRF TXM and the fitting result using *PyMCA* software.
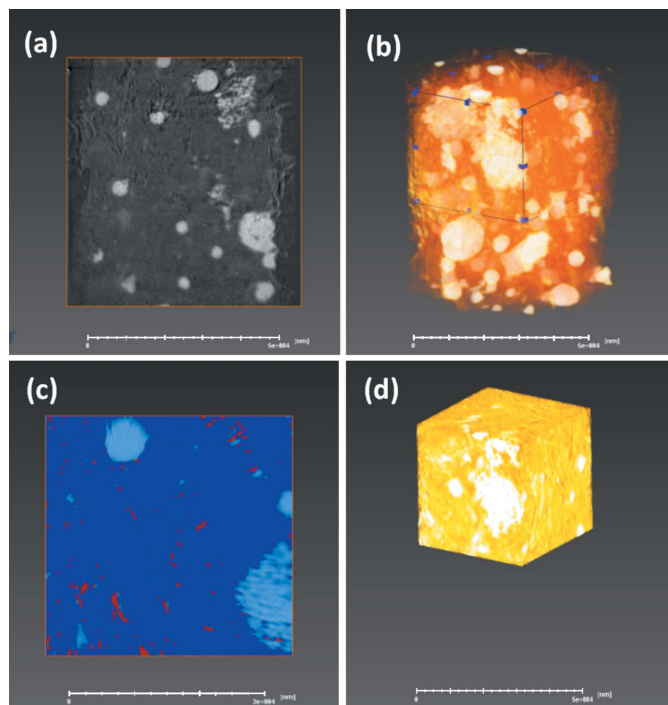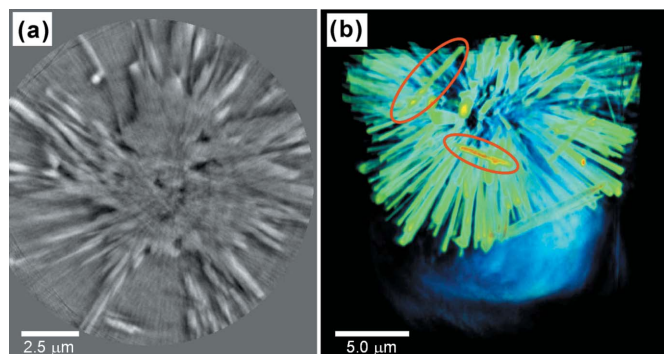
Figure 10
Reconstruction of the shale sample. The slice image and three-dimensional reconstruction of the shale sample are shown as (*a*) and (*b*). The two-dimensional and three-dimensional image segmentation of a part of the shale sample marked by the black box shown in (*b*) are shown as (*c*) and (*d*). The scale bars are 50 µm.

which may be extracted and converted into fossil fuel. It is believed that the stored energy may exist within the pore space, but the pores typically range in size from ~ 1 µm to ~ 10 nm, so conventional micro-computed tomography does not allow for visualization of these fine features. Fig. 10(*a*) presents a virtual slice image of the shale sample, in which the grey value of each pixel corresponds to the extent of the shift of X-ray phase and amplitude. The image, collected at 8 keV utilizing absorption contrast, demonstrates sufficient contrast and spatial resolution to differentiate individual pore segments (dark grey), quartz matrix (medium grey) and some inclusions (bright grey/white). The three-dimensional volume rendering of this result is also displayed in Fig. 10(*b*). Figs. 10(*c*) and 10(*d*) present the two-dimensional and three-dimensional image segmentation, respectively, of this sample, produced using the *Avizo Fire* software (Visualization Sciences Group, Bordeaux, France). According to the results of image segmentation, the quantitative volume for the pores, quartz matrix and inclusions are 1.58×10^{12} nm^3, 4.32×10^{12} nm^3 and 4.49×10^{12} nm^3, respectively, corresponding to a porosity of 3.20%.

Another sample is an assembled particle made of zinc silicate (Qu *et al.*, 2012), roughly spherical with a diameter of about 20 µm. This kind of hierarchical structured material is used as adsorbents in water treatment and catalyst applications and its internal structure influences the growth mechanism and corresponding chemical performance. However, because the sample is too thick for the transmission

Figure 11
Zernike phase-contrast X-ray tomography of a ZnSiO$_4$ particle showing (*a*) one reconstructed slice of the particle and (*b*) three-dimensional volume rendering.

of the TEM (transmission electron microscope) electron beam, it is difficult to observe the internal structure by TEM (Qu *et al.*, 2012). Using TXM with Zernike phase contrast at 8 keV, the true internal structure of the particle was successfully imaged, as shown in Fig. 11. From the virtual slice shown in Fig. 11(*a*), the interior of the sample can be clearly observed, while Fig. 11(*b*) shows some assembled defects, indicated with elliptical annotations. These show that some micro-rods are misaligned inside the regular micro-rod array, possibly reflecting improper processing parameters. The structures revealed by TXM may play a great role in the research and development of assembly conditions.

5. Conclusions

A high-resolution full-field transmission hard X-ray microscope with fluorescence mapping capability was constructed at the first-generation synchrotron facility BSRF. The beamline design criteria for the instrument are described in detail based on the transfer of phase space. Testing results give a spatial resolution of better than 30 nm and fluorescence sensitivity better than 50 p.p.m. The instrument is now entering user operation and will be put to use as a new tool in the fields of biology and materials science.

References

Andrews, J. C., Almeida, E., Meulen, M. C. H., Alwood, J. S., Lee, C., Liu, Y., Chen, J., Meirer, F., Feser, M., Gelb, J., Rudati, J., Tkachuk, A., Yun, W. & Pianetta, P. (2010*a*). *Microsc. Microanal.* **16**, 327–336.

research papers

Andrews, J. C., Brennan, S., Patty, C., Luening, K., Pianetta, P., Almeida, E., Meulen, M. C. H., Feser, M., Gelb, J., Rudati, J., Tkachuk, A. & Yun, W. (2008). *Synchrotron Rad. News*, **21**, 17–26.

Andrews, J. C., Meirer, F., Liu, Y., Mester, Z. & Pianetta, P. (2011). *Microsc. Res. Tech.* **74**, 671–681.

Andrews, J. C., Pianetta, P., Meirer, F., Chen, J., Almeida, E., van der Meulen, M. C., Alwood, J. S., Lee, C., Zhu, J. & Cui, Y. (2010*b*). *AIP Conf. Proc.* **1234**, 79–82.

Chen, T. Y., Chen, Y. T., Wang, C. L., Kempson, I. M., Lee, W. K., Chu, Y. S., Hwu, Y. & Margaritondo, G. (2011*a*). *Opt. Express*, **19**, 19919–19924.

Chen, Y. T., Chen, T. Y., Yi, J., Chu, Y. S., Lee, W. K., Wang, C. L., Kempson, I. M., Hwu, Y., Gajdosik, V. & Margaritondo, G. (2011*b*). *Opt. Lett.* **36**, 1269–1271.

Chen, H. H., Chien, C. C., Petibois, C., Wang, C. L., Chu, Y. S., Lai, S. F., Hua, T. E., Chen, Y. Y., Cai, X., Kempson, I. M., Hwu, Y. & Margaritondo, G. (2011*c*). *J. Nanobiotechnol.* **9**, 14.

Chen, J., Wu, C., Tian, J., Li, W., Yu, S. & Tian, Y. (2008). *Appl. Phys. Lett.* **92**, 233104.

Chichon, F. J., Rodriguez, M. J., Pereiro, E., Chiappi, M., Perdiguero, B., Guttmann, P., Werner, S., Rehbein, S., Schneider, G., Esteban, M. & Carrascosa, J. L. (2012). *J. Struct. Biol.* **177**, 202–211.

Chu, Y. S., Yi, J. M., De Carlo, F., Shen, Q., Lee, Wah-Keat, Wu, H. J., Wang, C. L., Wang, J. Y., Liu, C. J., Wang, C. H., Wu, S. R., Chien, C. C., Hwu, Y., Tkachuk, A., Yun, W., Feser, M., Liang, K. S., Yang, C. S., Je, J. H. & Margaritondo, G. (2008). *Appl. Phys. Lett.* **92**, 103119.

Feng, Y., Feser, M., Lyon, A., Rishton, S., Zeng, X., Chen, S., Sassolini, S. & Yun, W. (2007). *J. Vac. Sci. Technol. B*, **25**, 2004–2007.

Gordon, B. M. (1982). *Nucl. Instrum. Methods*, **204**, 223–229.

Hertz, H. M., Hofsten, O., Bertilson, M., Vogt, U., Holmberg, A., Reinspach, J., Martz, D., Selin, M., Christakou, A. E., Jerlstrom-Hultqvist, J. & Svard, S. (2012). *J. Struct. Biol.* **177**, 267–272.

Hsu, P. C., Chu, Y., Yi, J., Wang, C. L., Wu, S. R., Hwu, Y. & Margaritondo, G. (2010). *Appl. Phys. Lett.* **97**, 033101.

Jiang, J., Zhao, J., Tian, Y., Han, Y., Chao, Z., Jiang, X. & Xian, D. (1993). *Nucl. Instrum. Methods Phys. Res. A*, **336**, 354–360.

Liu, Y., Andrews, J. C., Meirer, F., Mehta, A., Gil, S. C., Sciau, P., Mester, Z. & Pianetta, P. (2011*a*). *AIP Conf. Proc.* **1365**, 357–360.

Liu, Y., Andrews, J. C., Wang, J., Meirer, F., Zhu, P., Wu, Z. & Pianetta, P. (2011*b*). *Opt. Express*, **19**, 540–545.

Meirer, F., Cabana, J., Liu, Y., Mehta, A., Andrews, J. C. & Pianetta, P. (2011). *J. Synchrotron Rad.* **18**, 773–781.

Nelson, G. J., Harris, W. M., Izzo, J. R. Jr, Grew, K. N., Chiu, W. K. S., Chu, Y. S., Yi, J., Andrews, J. C., Liu, Y. & Pianetta, P. (2011). *Appl. Phys. Lett.* **98**, 173109.

Qu, J., Cao, C., Hong, Y., Chen, C., Zhu, P., Song, W. & Wu, Z. (2012). *J. Mater. Chem.* **22**, 3562–3567.

Solé, V. A., Papillon, E., Cotte, M., Walter, P. & Susini, J. (2007). *Spectrochim. Acta B*, **62**, 63–68.

Sun, Y. & Wang, Y. (2011). *Nano Lett.* **11**, 4386–4392.

Tian, Y., Li, W., Chen, J., Liu, L., Liu, G., Tkachuk, A., Tian, J., Xiong, Y., Gelb, J., Hsu, G. & Yun, W. (2008). *Rev. Sci. Instrum.* **79**, 103708.

Tkachuk, A., Duewer, F., Cui, H., Feser, M., Wang, S. & Yun, W. (2007). *Z. Kristallogr.* **222**, 650–655.

Wang, J., Chen, Y. K., Yuan, Q., Tkachuk, A., Erdonmez, C., Hornberger, B. & Feser, M. (2012). *Appl. Phys. Lett.* **100**, 143107.

Wu, Z., Yun, W., Zhu, P., Wang, Y., Yuan, Q., Tkachuk, A., Huang, W. & Fester, M. (2010). US Patent 7 796 725 B1.

Yi, J., Chu, Y. S., Chen, Y. T., Chen, T. Y., Hwu, Y. & Margaritondo, G. (2011). *J. Phys. D*, **44**, 232001.

Yin, G.-C., Chen, F.-R., Hwu, Y., Shieh, H.-P. & Liang, K. (2007). *Appl. Phys. Lett.* **90**, 181118.

Yin, G.-C., Tang, M.-T., Song, Y.-F., Chen, F.-R., Liang, K. S., Duewer, F. W., Yun, W., Ko, C.-H. & Shieh, H.-P. D. (2006). *Appl. Phys. Lett.* **88**, 241115.

Zeng, X., Duewer, F., Feser, M., Huang, C., Lyon, A., Tkachuk, A. & Yun, W. (2008). *Appl. Opt.* **41**, 2376–2381.